Volume 3
Number 17
7 September 2021
Pages 4881–5124

Nanoscale Advances

rsc.li/nanoscale-advances

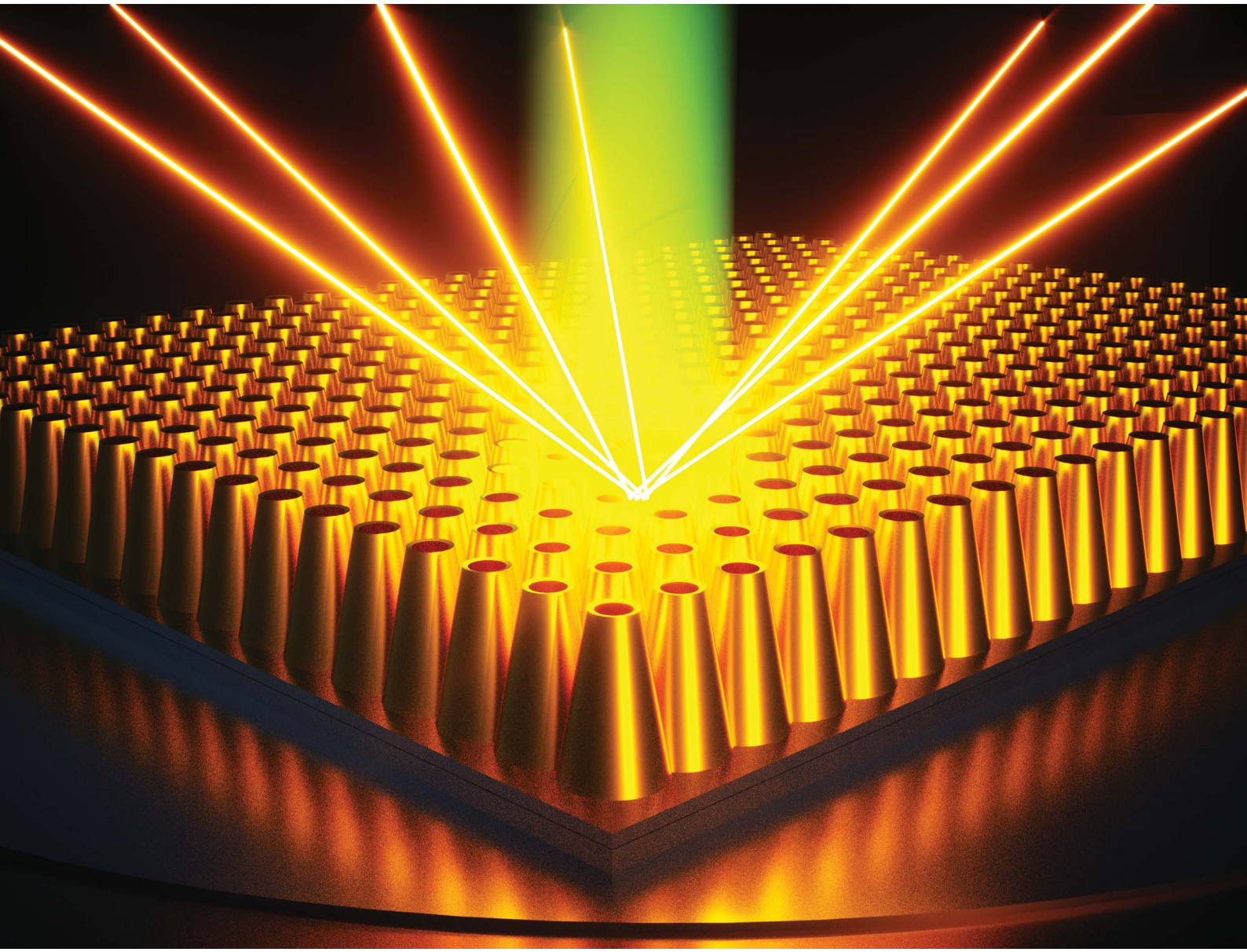

ISSN 2516-0230

ROYAL SOCIETY OF CHEMISTRY

PAPER
D. Jonker, I. De Leon, A. Susarrey-Arce *et al.*
A wafer-scale fabrication method for three-dimensional plasmonic hollow nanopillars

NCNST

Nanoscale Advances

ROYAL SOCIETY OF CHEMISTRY

PAPER

View Article Online
View Journal | View Issue

Cite this: *Nanoscale Adv.*, 2021, **3**, 4926

A wafer-scale fabrication method for three-dimensional plasmonic hollow nanopillars†

D. Jonker, ‡*[a] Z. Jafari, ‡[b] J. P. Winczewski,[a] C. Eyovge,[a] J. W. Berenschot,[a] N. R. Tas,[a] J. G. E. Gardeniers,[a] I. De Leon *[b] and A. Susarrey-Arce *[a]

Access to nanofabrication strategies for crafting three-dimensional plasmonic structures is limited. In this work, a fabrication strategy to produce 3D plasmonic hollow nanopillars (HNPs) using Talbot lithography and I-line photolithography is introduced. This method is named subtractive hybrid lithography (SHL), and permits intermixed usage of nano-and-macroscale patterns. Sputter-redeposition of gold (Au) on the SHL resist pattern yields large areas of dense periodic Au-HNPs. These Au-HNPs are arranged in a square unit cell with a 250 nm pitch. The carefully controlled fabrication process resulted in Au-HNPs with nanoscale dimensions over the Au-HNP dimensions such as an 80 ± 2 nm thick solid base with a 133 ± 4 nm diameter, and a 170 ± 10 nm high nano-rim with a 14 ± 3 nm sidewall rim-thickness. The plasmonic optical response is assessed with FDTD-modeling and reveals that the highest field enhancement is at the top of the hollow nanopillar rim. The modeled field enhancement factor (EF) is compared to the experimental analytical field enhancement factor, which shows to pair up with *ca.* $10^3 <$ EF $< 10^4$ and *ca.* $10^3 <$ EF $< 10^5$ for excitation wavelengths of 633 and 785 nm. From a broader perspective, our results can stimulate the use of Au-HNPs in the fields of plasmonic sensors and spectroscopy.

Received 28th April 2021
Accepted 7th July 2021

DOI: 10.1039/d1na00316j

rsc.li/nanoscale-advances

1. Introduction

Metallic nanostructures are well known for their potential to concentrate electromagnetic fields to nanometric volumes, particularly at optical wavelengths. This is possible due to the excitation of surface plasmon resonances supported by such structures.[1,2] The large optical intensities resulting from the strong field concentration around plasmonic nanostructures lead to the enhancement of light–matter interactions, which are of particular interest for optical sensing.[3–7] In this case, localized surface plasmon resonance constitutes a versatile technique that exploits the sensitivity of plasmonic structures to a small change in the refractive index caused by (bio)molecules or more complex systems like polymers near the nanostructure vicinity.[8–10] In Raman spectroscopy, surface plasmon resonances contribute dominantly to the excitation of vibrational modes of molecules near metallic surfaces, giving rise to the phenomenon known as surface-enhanced Raman spectroscopy (SERS).[11,12] The resonance frequency and modal behavior of the nanostructured surface can be fine-tuned by controlling the surface morphology of a collection of structures and the physical and/or chemical composition of a single structure.[13–15] This includes randomly assembled and well-arranged nanoparticle systems configured in the form of dimers, trimers, or higher in geometrical order, coherently contributing to an enhanced Raman signal.[16–22]

Bottom-up or top-down nanofabrication processes can offer large-scale manufacturing of nanoplasmonic sensors.[23–26] A key element for manufacturing well-organized multidimensional nanoplasmonic substrates is implementing patterning steps. Well-known patterning steps include colloidal lithography,[27,28] nanoimprint lithography (NIL),[29] charged beam lithography,[30] and photolithography.[31,32] Each technique has its limitations, as there is usually a trade-off between resolution, pattern design versatility (to be called "pattern-ability" here), time consumption, and cost. For instance, colloidal lithography relies on colloidal particle assembly, restricting the mask pattern to the colloidal packing morphology providing limited pattern-ability.[33,34] Using template-assisted self-assembly, the colloidal packing morphology proves to be tunable with the final oligomer morphology being dependent on the template morphology.[35] Recent advances show that colloidal self-assembly in an electrohydrodynamic flow yields oligomers that form 3D porous media with good control over the nanoscale gaps at the macroscale.[36] Adding complexity to 2D patterning, multiparticle patterns can be achieved on a pre-

[a]*Mesoscale Chemical Systems, MESA+ Institute, University of Twente, PO. Box 217, Enschede 7500AE, The Netherlands. E-mail: d.jonker@utwente.nl; a.susarreyarce@utwente.nl*

[b]*School of Engineering and Sciences, Tecnologico de Monterrey, Monterrey, Nuevo Leon 64849, Mexico. E-mail: ideleon@tec.mx*

† Electronic supplementary information (ESI) available. See DOI: 10.1039/d1na00316j

‡ These authors contributed equally.

patterned substrate using a printing strategy based on a colloidal suspension confined by the meniscus of a capillary bridge.[37] NIL, on the other hand, is more versatile in the choice of 2D feature patterns. However, it relies on the design and fabrication of stamps, which can be tedious and therefore very costly to make.[29] Furthermore, the original stamp is fabricated by less straightforward patterning techniques and is prone to mechanical wear. Charged beam lithography methods, including approaches like electron- or ion beam lithography, provide spatial resolution below 10 nm,[38] although writing over large areas, *e.g.*, a wafer can be time-consuming.[39,40]

Conventional (UV) I-line photolithography is known for the ability to pattern a masking layer rapidly, but the technique has limited resolution when approaching nanoscale dimensions because of the diffraction limit.[31,32] To push the boundaries imposed by the diffraction limit, users can turn to an excimer laser for extreme UV exposures. Such machines are cost-intensive and not accessible for rapid-prototype fabrication purposes. Recent developments in photolithography omit the diffraction limit by utilizing electromagnetic interference to increase resolution, enabling sub-100 nm patterns in conventional I-line type resists.[41] Specifically, displacement Talbot lithography (DTL) utilizes the self-image generated by exposing a periodic phase-shift mask with a monochromatic light source. Periodic translation across an axis of the three-dimensional interference pattern, called the Talbot pattern, generally makes the patterning step insensitive to wafer-scale height variations. Therefore, DTL delivers highly uniform periodic nanopatterns at the wafer-scale.[42–45] Nevertheless, a missing element in DTL is the ability to confine a full wafer scale nanopattern onto selected areas over a substrate without the need for an adjusted DTL-mask.[45]

The aforementioned nanolithography techniques offer a plethora of possibilities to control the geometrical parameters of two-dimensional,[46–49] or three-dimensional nanostructures.[5,50–55] Nevertheless, a remaining challenge is achieving highly reproducible structural features over both wafer- and nanoscopic scales.[55]

In this work, a large area nanofabrication approach based on a novel combination of DTL and subtractive hybrid lithography (DTL/SHL) for selective patterning is presented. The DTL/SHL is proven useful as it benefits from the best aspects of the two lithography techniques, *e.g.,* resolution, rapidness, patternability, cost-effectiveness, and a single mask layer.[56,57] Such assets are important to the field of nanoelectronics,[58] nanosensing,[59–61] and nanofluidics.[62,63] Our DTL/SHL method employs a single photoresist and two exposure techniques to generate a nanopatterned photoresist and bottom anti-reflective coating (BARC) in the form of nanopillar-like structures at particular substrate locations. These nanopillars act as a template for the sidewall redeposition of Au during angled ion beam etching (IBE). An angled etching step during IBE controls the redeposition rate, different from IBE performed at normal incidence reported in other studies.[53,54,64] Stripping the BARC-photoresist yields a cavity, giving rise to uniformly distributed Au-HNPs at the wafer-scale over a titanium coated (Ti)-glass substrate with low poly-dispersity of the structural dimensions. The fabrication procedure enables control over the different length scales with 14 ± 3 nm sidewall rims, and a 250 nm pitch in a square lattice while the DTL/SHL technique provides the basis for device integration at the μm to cm-scale. As a proof of concept, the optical response of the fabricated Au-HNP arrays is evaluated with UV-VIS-NIR and Raman spectroscopy to experimentally derive the absorptance spectra and analytical enhancement factor (AEF). The experimental results are compared with the numerical results obtained through three-dimensional (3D) finite difference time domain (FDTD) simulations. Our numerical analysis shows good agreement with the experimental results and indicates dipolar and quadrupolar plasmonic resonances dominating visible and NIR portions of the spectrum. It is demonstrated that the dipolar resonance is blueshifted by ~90 nm whenever the BARC is stripped with an oxygen plasma, providing a degree of freedom for plasmonic resonance-tuning and showing sensing capabilities of the Au-HNP interior. The numerically calculated EF and AEF are also in good agreement with *ca.* $10^3 < EF < 10^4$ and *ca.* $10^3 < EF < 10^5$ for excitation wavelengths (λ_{ex}) of 633 and 785 nm. The results demonstrate a good correlation between FDTD-simulations and optical experiments.

2. Methods

2.1. Nanofabrication of Au-HNPs

2.1.1 Metal deposition and patterning periodic dotted nanostructures in BARC. A 100 mm diameter 500 μm thick glass substrate (MEMpax®, SCHOTT technical glass solutions) was selected, and 13, 20, and 40 nm of titanium (Ti) layers were sputter-deposited in Argon (Ar) at 200 W power (T'COathy, home-built at MESA+ institute) and a pressure of 0.66 Pa. Subsequently, without breaking the vacuum, an 80 nm thick Au-layer was deposited over each Ti thickness with the same sputtering power and pressure.

The MEMpax® Ti/Au substrate was spin-coated with an anti-reflective coating (BARC, Barli-II, AZ Microchemicals) at 3000 rpm for 45 s. After spin-coating, the film was pre-baked for 90 s at 185 °C, yielding an ~196 nm thick BARC film. A positive tone I-line photoresist (PFI-88a, PGMEA 1 : 1, Sumitomo) was then spun on top of the BARC layer at 2000 rpm for 45 s and pre-baked at 90 °C for 90 s, yielding a 297 nm thick I-line photoresist layer. Mask nanopatterning of the BARC and I-line photoresist was initiated by performing oDTL (PhableR 100C, EULITHA) by exposing the resist twice for 45 s at the exposure wavelength of 375 nm with 0.98 mW cm^{-2} intensity. Between light exposures, the substrate was rotated 90°. SHL was achieved by a sequential tertiary I-line exposure over a conventional chrome photomask employing a mask-aligner (EVG 620, EV Group) and conducting the exposure at 365 nm wavelength with 12.0 mW cm^{-2} for 6.5 s. A post-exposure bake was performed at 110 °C for 90 s. The PFI film was sequentially developed in a solution of TMAH (OPD4262, Arch Chemicals) by submerging the substrate two times for 30 s in separate beakers, rinsing in a quick-dump rinser, and spin-drying. This method gives rise to a patterned PFI layer consisting of 90 nm diameter dots organized in a square lattice unit cell with a 250 nm pitch over the BARC

layer. Note that the BARC/PFI layers are named BARC only for simplicity.

2.1.2 Patterning of BARC. The directional transfer of the patterned PFI into the BARC layer (hereafter BARC) was achieved by applying a reactive ion etching step (RIE) to the substrate in a conductively coupled plasma RIE system (TEtske, Home-built MESA+). Before the RIE was applied, the plasma chamber was first cleaned by wiping with acetone and IPA, after which an oxygen plasma cleaning was performed for 10 minutes at 100 W, 6.7 Pa of pressure, and 50 sccm O_2 flow. Finally, the chamber was conditioned with a nitrogen flow under the process conditions for five minutes to reduce the remaining oxygen in the gas supply lines. Note that conditioning the chamber reduces substrate-to-substrate variation between the first processed substrates because residual oxygen can etch the BARC isotropically. Then, the RIE was conducted in a nitrogen (N_2) plasma under process conditions using a 50 sccm N_2 flow, 25 W applied power, and 1.7 Pa of applied pressure yielding a DC bias of ~290 V. The RIE step lasted for 8 minutes. In all RIE steps, the pressure in the plasma chamber was reduced to the base value lower than 0.66 Pa before the initiation of the process. After the plasma process, the formation of nanocolumn arrays made out of BARC was completed.

2.1.3 Nanofabrication of hollow pillars with IBE. The substrate with BARC patterned nanocolumns on the Ti/Au layer was transferred into the ion beam etcher (Ion fab i300system, Oxford Instruments), which works at a base pressure of $\sim 3 \times 10^{-5}$ Pa. After substrate transfer and clamping, 660 Pa of gas pressure was applied to give a volumetric flow of 1.1 sccm of Helium for backside cooling. 5 sccm of Ar-flow was supplied to both the plasma and process chamber. The process pressure was measured to be ~0.03 Pa. Then, the plasma process was initiated by first igniting the plasma, and limiting the applied power of the RF generator to 300 W. Once the ignition was successful, a 300 V acceleration potential was applied between the plasma and a mesh grid to accelerate the Ar^+ ions towards the substrate. During Ar^+ bombardment, the substrate was rotated with a rotational speed of 5 rpm, while the surface normal of the substrate was kept at a 20-degree angle relative to the surface normal of the acceleration grid. Secondary ion mass spectroscopy was used to monitor the material removal during IBE.

2.1.4 Stripping of the BARC template. Stripping of the BARC after the sidewall redeposition of Au was achieved by RIE. An RIE step in O_2 for 8 minutes at 25 W, 1.7 Pa pressure, and 50 sccm O_2 flow was performed on the TEtske to remove the BARC nanocolumns leaving the Au-HNPs over the Ti coated MEMpax® substrate.

2.2 TEM sample preparation

A substrate containing Au-HNPs was transferred into a vacuum system where a 20 nm thick carbon film was sputter-deposited. Next, the sample was transferred into a high vacuum chamber where, at first, a ~3 μm Pt layer was deposited at the location of interest by Ga^+ assisted chemical vapour deposition. Sequentially, an SEM assisted dual-beam focused ion beam (Nova 600 Nanolab Dual-beam SEM/FIB, FEI) was used to cut out a ~ 1 μm thin, 15 μm long sample from the device area using a 30 kV Ga^+ ion beam. The axis along which the cut was performed was at approximately 4.8 degrees with the primary axis of the square unit cell. Just before the TEM sample be released from the substrate, a wire was welded to the Pt layer by Ga^+ assisted chemical vapour deposition. The sample was released, transferred to a TEM grid, and attached again. The wire was removed by milling the weld. Finally, the sample was additionally thinned to 50 ± 10 nm, yielding a thin foil. Because of the angle between the cut and the primitive axis of the square unit cell, there was an intersection with the Au-HNP every 12 periods.

2.3 SEM sample preparation

After optical measurements, the sample was diced with a wire cutter, intersecting the device area. Parts of the fragmented sample were mounted on a stainless-steel sample carrier either in an upright position or flat position and transferred into the HR-SEM system (Merlin, Zeiss) for both cross-sectional and topside inspection.

2.4 Optical measurements

The optical characterization was performed with a UV-VIS-NIR-spectrophotometer (PerkinElmer Lambda 950 UV-vis–NIR) between 250 and 1200 nm with the integrating sphere. The transmittance (T) spectrum and the reflectance (R) spectrum were collected separately to estimate the absorptance (A) of the structured substrates. Similarly, the T and R for non-structured substrates, such as Ti-deposited and Ti/Au-deposited flat substrates, were also recorded. The absorptance spectra were calculated using eqn (1) given below.

$$A = 1 - (T + R) \quad (1)$$

2.5 Numerical modelling of the optical response

The optical response of the Au-HNPs was numerically calculated using a 3D FDTD solver (Lumerical). To calculate the absorption cross-section, a linearly polarized total-field/scattered-field source was used to illuminate an isolated Au-HNP. A perfectly matched layer (PML) boundary condition was used for all boundaries. A box of power monitors surrounded the isolated Au-HNP. The absorption cross-section was found by the power sunk into the box of monitors divided by the source intensity. Large periodic arrays of Au-HNPs were also simulated with 3D FDTD. In this case, only one unit cell was modeled with periodic boundary conditions on all the transversal sides and PML boundary conditions on the longitudinal boundaries (top and bottom of the unit-cell). A linearly polarized plane-wave source illuminated the samples. The mesh size over the Au-HNPs was as small as $dx = dy = 2$ nm in the transverse plane, and $dz = 5$ nm along with the Au-HNP height. Mesh override regions with a smaller mesh size along the z-direction ($dz = 1$ nm) were used at the sharp corners or curvatures (*i.e.* at the nano-rim and the bottom of the hollow section) to avoid spurious hot-spots. Finally, transmittance and reflectance were found by using

two power monitors, and the absorbance was calculated according to eqn (1).

2.6 Raman enhancement factor

2.6.1 Measurement protocol. An Alpha 300 Confocal Raman Microscope (WITec, Ulm, Germany) equipped with an MPlan FL N 100×/0.9 NA air objective (Olympus, Tokyo, Japan) was used. SERS spectra were collected in backscattering geometry.

The integration time, laser power, spectral resolution, and the number of accumulations for each presented spectrum were 10 s, 0.5 mW, 2 cm^{-1}, and three times, respectively. Prior to SERS measurements, the SERS substrates and flat reference layers of Au on Ti were incubated separately for 24 hours in 1 mM aqueous solution of Methylene blue trihydrate (MB, Alfa Aesar). The SERS substrates were left in a vertical position, rinsed with ultrapure water, and dried in a nitrogen stream.

2.6.2 Analysis of Raman data. The presented SERS and Raman spectra have been baseline corrected using an asymmetric least squares smoothing algorithm and averaged by a moving average filter with a window of size 7.[65] The peaks were extracted by first using peak detection based on a filtered first derivative zero pass algorithm and afterwards, a peak fitting algorithm.[66] The threshold for a detected peak was larger than 1/4 of the maximum value within a recorded spectrum. Peak assignment is shown in Tables S3 and S4,† Section 3 of the ESI files.

2.6.3 Raman enhancement factor. The AEF is calculated by relating the area of the peak intensity of the surface coated MB, I_{SERS}, to the peak intensity of the MB in solution, I_{BULK}, while also considering the number of molecules probed on the surface, N_{SERS}, and those in a small volume inside the solution, N_{BULK}.[67]

$$AEF = (I_{SERS}/N_{SERS})/(I_{BULK}/N_{BULK}) \quad (2)$$

N_{BULK} was calculated by considering the interaction volume of the excitation laser source and the solution concentration, c_{sol}, through:

$$N_{BULK} = N_A \times c_{sol} \times A_{beam} \times h_{eff} \quad (3)$$

where A_{beam} is the area of the beam waist at the focal spot and h_{eff} is the interaction length of the excitation laser. N_A is the Avogadro constant. The interaction length of the laser is calculated by assuming that the area under a Gaussian distributed normalized intensity in the axis parallel to the axis of light propagation, $I(z)$, is equal to that of a thin disk of height, h_{eff}, and normalized peak intensity, I_0:

$$h_{eff} \times I_0 = \int_{-\infty}^{\infty} I(z)dz \quad (4)$$

In a real measurement setup, this translates to recording SERS spectra at discrete positions around the location where the optical focal point coincides with the substrate and calculating the total intensity of a known Raman peak over a fixed interval. In this case, measurements were conducted on a flat single crystalline silicon surface (001) in the $495 < k < 545$ cm^{-1} band. Spectra were recorded moving with steps of 0.5 μm within a maximum range of ±5 μm close and perpendicular to the substrate, so that

$$I(z) = \sum_{k=495}^{545} I_k \quad (5)$$

where I_k is the recorded intensity in arbitrary units at a certain wavenumber. The results of this analysis are shown in Fig. S15.† For a 633 nm excitation at 100× magnification, 0.9 numerical aperture, and 0.5 mW of power, the interaction length was calculated to be 1.52 μm.

To determine N_{SERS}, one needs to find the surface density of MB molecules. Hence, we consider a monolayer coverage for this analysis. The surface density is found by considering the surface area per MB molecule, A_{sm}. We have found different values across the literature. Narband *et al.*[68] estimated A_{sm} based on space-filling, covalent radius, or van der Waals radius to be, 1.01 nm^2, 0.66 nm^2, or 3.75 nm^2, respectively.[68] Hang *et al.*[69] found an A_{sm} of 1.3 nm^2 and dimensions 17.0 × 7.6 × 3.25 Å based on various sources.[69] Song *et al.*[70] conducted STM measurements on Au (111) surfaces and found an A_{sm} of 3.5 nm^2 (2.5 × 1.4 nm^2 unit cell).[70] The choice was made to accept the value measured by Song *et al.*[70] as it is the only direct measurement delivering an image of the MB morphology on Au. Finally, to calculate N_{SERS}, the surface density of molecules adhered to the surface, ${A_{sm}}^{-1}$, is multiplied with the total surface area:

$$N_{SERS} = \frac{G}{A_{sm}} A_{beam} \quad (6)$$

where G is a structure factor that relates the surface area of the Au-HNP, $A_{HNP} = 29.9 \times 10^4$ nm^2, calculated from the dimensions shown in Fig. S7,† assuming cylindrical symmetry, to the area of a square unit cell with a length of 250 nm, $A_{UC} = 6.25 \times 10^4$ nm^2, yielding $G = A_{HNP}/A_{UC}$. The final expression is found by plugging eqn (3) and (6) into eqn (2), giving:

$$AEF = \frac{I_{SERS}}{I_{BULK}} \times \frac{N_A c_{sol} h_{eff} A_{sm}}{G} \times \frac{A_{beam}}{A_{beam}} = 713 \times \frac{I_{SERS}}{I_{BULK}} \quad (7)$$

An example of the extracted peak areas of a droplet-based measurement and a substrate-based measurement is shown in Fig. S16.†

3. Results and discussions

3.1 Fabrication of Au hollow nanopillars by sputter redeposition on a hybrid mask

3.1.1 Hybrid patterning. The DTL/SHL fabrication is a novel approach to pattern a single photoresist layer at different length scales. Combining the SHL derived resist template with an ion beam sputter redeposition and sequential removal of the resist template results in Au-HNPs that are easily integrated into a plasmonic device. The nanofabrication of Au-HNPs was initiated at the wafer-scale by Ti and Au sputter-deposition on a glass substrate, Fig. 1(a)–(c). The Ti-layer

thickness was either 13, 20, or 40 nm, while the Au layer thickness was maintained at 80 nm. The BARC was spin-coated on top of the Au, followed by the deposition of a positive tone photoresist (PFI), Fig. 1(d) and (e). Next, the resist was exposed twice, employing orthogonal DTL under a 500 nm pitch line-pattern phase-shift mask. 90 degrees rotation between two subsequent DTL exposures and subsequent development of the resist yield the full-wafer scale nanodot resist pattern as schematically shown in top-view Fig. 1(f) and side-view imaged in Fig. S1,† with PFI dots being 100 nm in diameter. Note that, hereafter, the BARC/PFI layers and nanopillar pattern in Fig. 1(f) and (g) are named BARC for simplicity.

The SHL step is then introduced for substrate fabrication. The hybrid step is conducted between steps (e) and (f) in Fig. 1 and schematically presented in Fig. 2(a) and (b). It consists of a tertiary exposure of the resist in an I-line UV source under a conventional chrome photomask (Fig. 2(b)) before development. The advantage of using the SHL is the fast and selective patterning over several μm^2 to a full wafer scale within a few seconds of exposure (*ca.* 6 s). The pattern's final shape and size are limited by the chrome photomask resolution and the exposure wavelength.

Next, reactive ion etching (RIE) in N_2 plasma is used to pattern the BARC layer, partially exposing the Au surface (Fig. 1(g) and (2d)). Scanning electron microscopy (SEM) images of the BARC columns collected after transferring the hybrid resist pattern into the BARC layer are presented in Fig. 2(e)–(f). The SEM cross-section and top-view were recorded at the edge of the SHL nanopattern (see red arrow). Note that the nanodot pattern needs approximately 5 periods to become uniform. Thus, a trade-off exists between the rapidness and patternability *versus* the edge effects observed while employing SHL (Fig. 2).

3.1.2 Sputter redeposition. After patterning the BARC nanopillars and partially exposing the Au layer (Fig. 1(g) and 2(d)), the substrate was placed in an IBE system and exposed to an Ar^+ ion beam at a 20-degree angle and a 300 V acceleration potential for the sputter redeposition of Au (Fig. 1(h) and (i)). The side-view SEM image in Fig. 3(a) shows the obtained nanostructure containing a BARC core and sputter-redeposited Au at the sidewall. When etching the Au, the incident Ar^+ ions impact both the mask material and the exposed Au layer (Fig. 1(g)). For the exposed Au, Ar^+ ions can effectively etch the Au layer, which in turn sputter redeposits over the BARC-nanopillar sidewall.[71] Sidewall redeposition is governed by the incident – (i) ion energy, (ii) ion flux, and (iii) incident angle of ions during IBE. These parameters are connected to the sputtered material properties and crystallinity, directly impacting the etch-rate.[72,73] Selective redeposition at the sidewall over different geometries and compositions can be obtained.[72–74] Generally, the Au etch-rate with Ar^+ at 300 eV is higher closer to the normal incidence angle with respect to the surface. This is different from other materials, where usually an optimum incidence angle is found at oblique angles.[73] For nanostructures, the substrate incidence angle is different from that on the sidewall. In the case of the Au-HNP, the etch rate on the substrate is larger than that of the sidewall whenever the substrate incidence angle is smaller than 45 degrees. Indeed we observe the sidewall redeposition rate to be higher than the Au etch-rate at the BARC-nanopillar sidewall because the Au-HNP growth is achieved. This is a different mechanism than those reported in other studies where the etching was performed at normal incidence.[53,54,64,75] In this work, tuning the incidence angle can yield different etch rates on the substrate and sidewalls and thus yield varying redeposition rates. Moreover, for atomically flat surfaces at normal incidence, redeposition depends on the ion's mean free path length in the process chamber.[75] This is an extreme example, but it suggests that IBE at normal incidence only enables redeposition whenever the initial deposited material already has some roughness. Control over the redeposition rate is critical for the Au-HNP plasmonic structures. The sidewall thickness is important

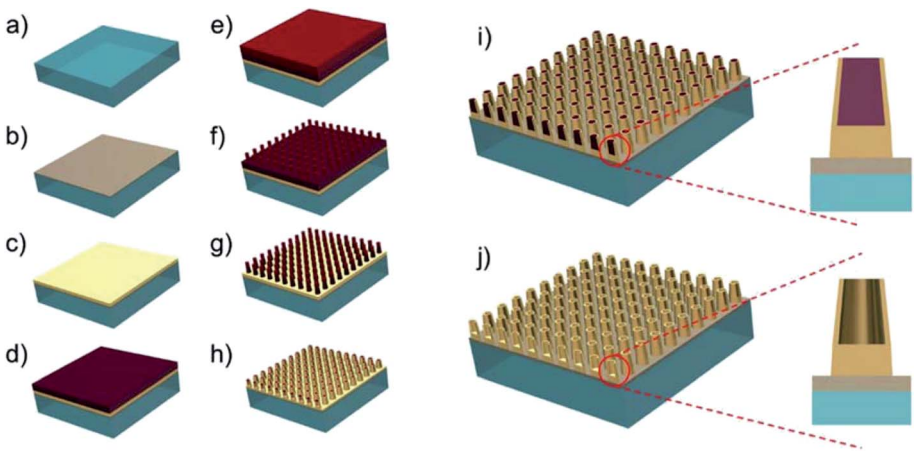

Fig. 1 Schematic representation of the nanofabrication steps for the production of the Au-HNP array. (a) MEMpax® substrate. (b) sputter deposition of different Ti thicknesses (13, 20, or 40 nm). (c) Sputter deposition of 80 nm of Au. (d) Spin coating of BARC. (e) Spin coating of PFI. (f) DTL patterning over BARC. (g) Nanopillar formation with RIE of BARC. (h) Side-wall deposition of Au over the nanopillars during angled IBE-cycles. (i) Au coated nanopillar, with a zoom-in cross-section. (j) Au-HNPs after BARC removal, with zoom-in cross-section.

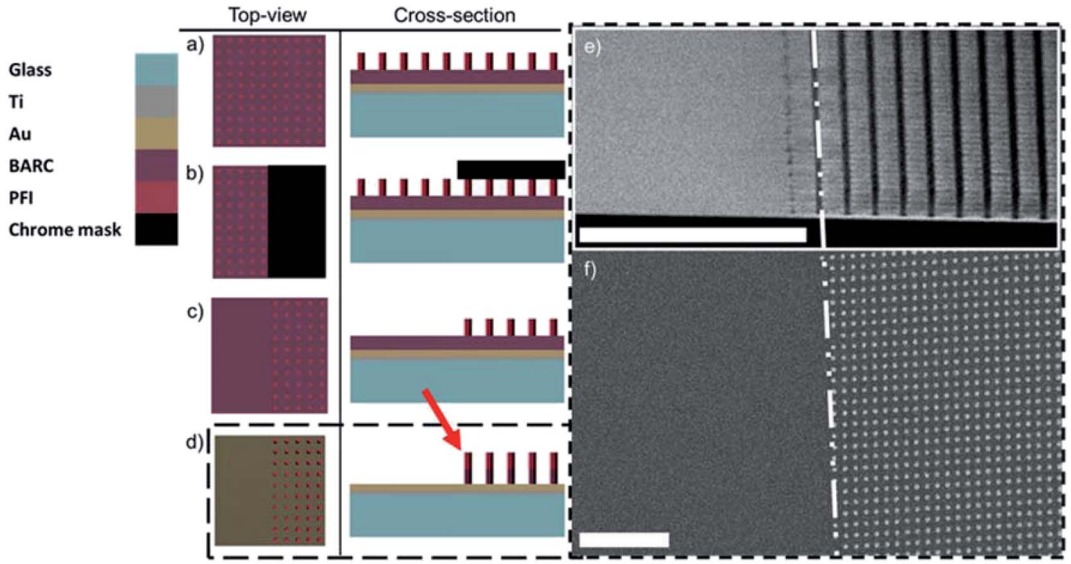

Fig. 2 The left (a)–(d) scheme illustrates part of the process flow by a schematic representation of the top- and cross-section view after the sequential application of the fabrication steps. (a) DTL of PFI; (b) tertiary exposure under a conventional photomask; (c) post-bake and development of PFI; (d) directional RIE of BARC in N_2 plasma. A legend is added relating the colors used in the schematics to the corresponding materials. SEM images on the right contain two micrographs of the substrate, after step (d). (e) and (f) images show the transition between the (un) masked area resulting from the tertiary exposure and RIE of BARC. (e) displays an image of the cross-section containing the BARC hybrid mask columns and (f) a top-view. The scale bars represent 2 μm.

for the plasmonic response, as shown in this article in the FDTD-section below.

After Au sputter-redeposition over the BARC-nanopillars, the last step is to remove the remaining BARC inside the Au-HNP. The removal of the BARC layer is carried out by applying an oxygen (O_2) plasma. Characterization of the plasma treatment is performed in a plasma asher and an RIE setup. For increased applied powers and prolonged-time, removing the BARC

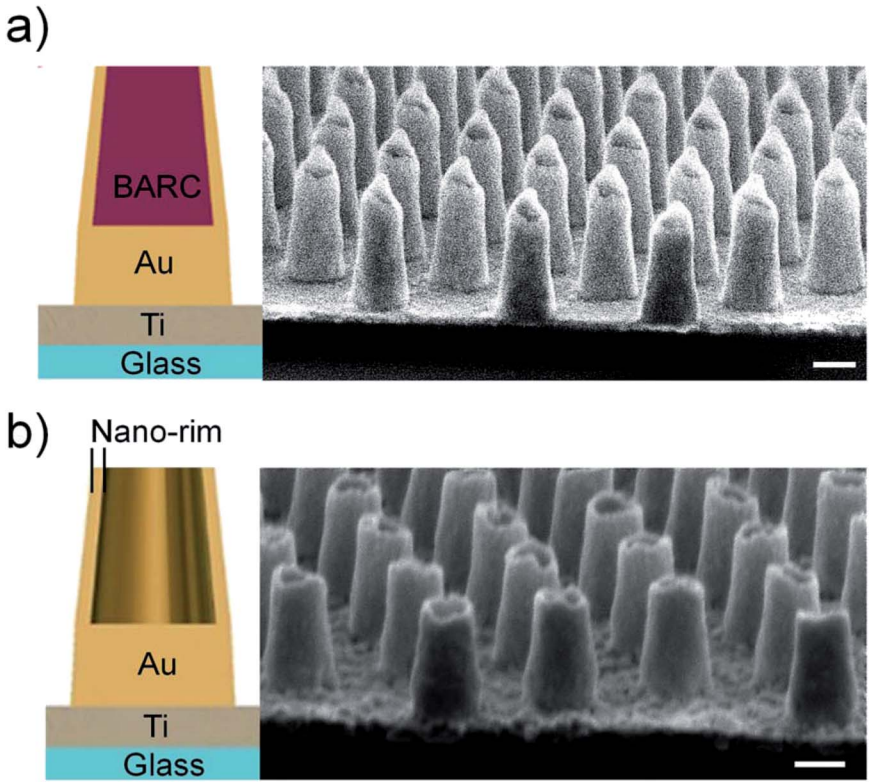

Fig. 3 (a) Au-HNPs with BARC and (b) Au-HNPs without BARC. Each SEM image is accompanied by a schematic representation of the nanofabricated Au structures. The scale bar is 100 nm.

negatively affects the structural integrity of the Au-HNP, as can be seen in Fig. S2.† The prolonged exposure to the high power plasma introduces a high surface temperature and sintering effect, as observed by the polycrystalline domains reforming into larger grains. An optimum time for O_2 plasma etching is found to be 8 min at 25 W. This step delivers an array of Au-HNPs with structural integrity, as shown in Fig. 3(b) and S3.† Images of wafer-scale fabricated substrates with and without BARC are presented in Fig. S4.†

3.1.3 Au hollow nanopillar composition and morphology. The structural and chemical characteristics of the Au-HNPs are assessed before detailed optical analysis. In Fig. 4(a) and (b), a TEM cross-section image of Au-HNPs and a close-up to one of the top edges are shown which were recorded after removal of the BARC template thus displaying empty cavities inside the Au-HNP. The dashed red box over the Au edge indicates the location of the fast Fourier transform, confirming Au (111) planes. A high degree of polycrystallinity over the fabricated Au-HNPs with various grain sizes is also observed between the bottom solid and top nano-rim structure. It is believed that this variance in grain sizes is responsible for the observed roughness at the nano-rim. In this case, no effort was made to improve the roughness by applying, for instance, a planarizing film and sequential angled IBE under a large angle.[76,77] The difficulty in implementing such planarization steps would be to find a polymer coating that is not too thick but shows a good step-coverage. Additionally, in the cited studies, R_a roughness values of a few nanometers were reduced to several angstroms, however, considering significant etch depths of 300 nm.

Chemical composition from the energy-filtered TEM in Fig. 4(c)–(f) indicates carbon (C) in red, oxygen (O) in blue, titanium (Ti) in white, and Au in yellow. Brighter white/grey color contrast reveals the presence of C. This is expected as the C is evaporated during sample preparation for TEM. Dimer white/grey color contrast is also found for Ti and O over the Au-HNP, suggesting a thin oxidized titanium layer, possibly of TiO_2. The presence of Ti is due to the exposure of the adhesion layer to Ar^+ during IBE. The O layer possibly forms throughout air exposure or BARC removal from the Au-HNPs.

The Au-HNP structure is subdivided into a solid base structure with the same thickness as that of the initially sputter-deposited 80 ± 2 nm Au layer and a 170 ± 10 nm high nano-rim structure. In Fig. 3(a) and (b), the total Au-HNP height, base plus nano-rim, is ~250 ± 12 nm, with a thin rim at the top. The outer base diameter was measured using top-view HR-SEM images with results shown in Fig. S5 and S6.† The particle dispersion based on the outer base dimension is 133 ± 4 nm. Note that the values were measured from different substrates and thus yielded batch-to-batch and location-to-location variation. Measurements of the inner nano-rim diameter conducted with TEM, shown in Fig. 4, reveal that the top of the Au-HNPs has a thin nano-rim of *ca.* 14 nm ± 3 nm. A schematic illustration containing all the Au-HNP dimensions extracted from the TEM images is displayed in Fig. S7.† It is worth noting that previous studies have already shown that ion beam redeposition on a photoresist mask can be used for patterning purposes. However, this work facilitates periodic organization with lattice constants small enough to be relevant for nanoplasmonics, which is different from that in Desbiolles *et al.*[51] Furthermore, we achieved patterning of sidewall structure with resolutions of ±3 nm. In this respect, Jeon *et al.*[50] achieved similar 3D architectures with NIL, but in our case, we have pattern-ability by SHL and show the wafer-scale homogeneity. Lastly, Mehrvar *et al.*[75] showed the complexity of using a capacitively coupled RIE for sidewall redeposition. Utilizing an IBE gives a more controllable platform for sidewall redeposition. The DTL/SHL

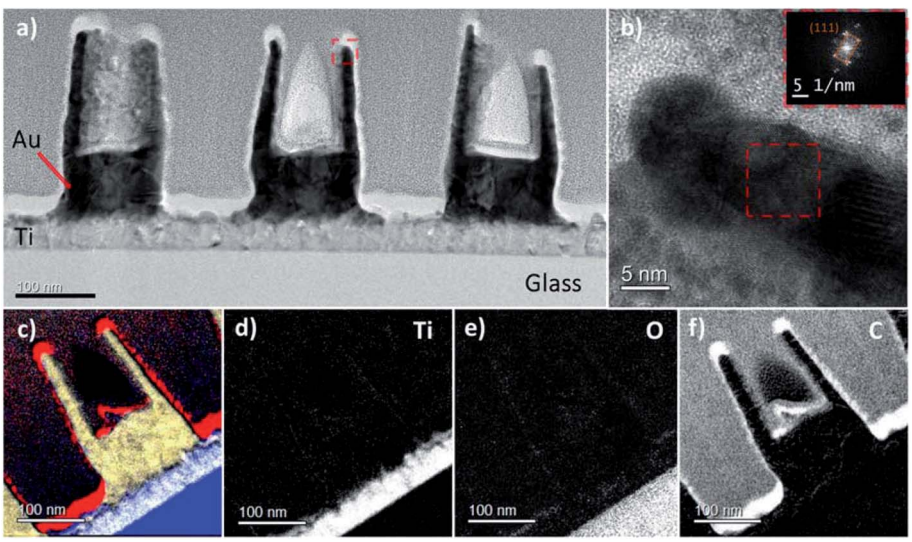

Fig. 4 (a) TEM image of as-fabricated Au-HNPs. Scale bar reads 100 nm. (b) Close-up to one of the top edges of the Au-HNPs. The scale bar represents 5 nm. The dashed box indicates the location of the processed FFT inset. The inset scale bar represents 5 nm^{-1}. (c) Color image representation overlaying the elemental profiles, extracted from the EF-TEM analysis, displayed in (d)–(f). In (c), red indicates carbon, blue oxygen, white titanium, and yellow indicate gold. Energy-filtered TEM image for (d) titanium, (e) oxygen, and (f) carbon. (c)–(f) scale bars represent 100 nm.

and angled IBE combination is necessary for device integration with well-defined plasmonic nanostructures, paving the way for complex device integration at the wafer scale.

3.2 Optical properties of the Au-HNP array

FDTD simulations for 3D Au-HNPs are performed to understand the optical response of the fabricated plasmonic array. The Au-HNP dimensions used in the numerical simulations are extracted from SEM and TEM images, summarized in Fig. S7.† First, the absorption cross-section of an isolated Au-HNP is calculated for two different cases, with and without BARC. It is noteworthy that BARC is located at the cavity of the Au-HNP (Fig. 3). Two peaks are observed in the absorption cross-section, as shown in Fig. 5(a) and (b). A charge distribution analysis is carried out to identify the supported modes of the Au-HNP at the peak wavelengths. The peak at longer wavelengths, *i.e.*, ~730 nm for Au-HNP with BARC and ~650 nm for Au-HNP without BARC, corresponds to the electric-dipole resonance formed by the horizontal charge separation at the rim of the Au-HNP (right inset in Fig. 5(a) and (b)). This type of resonance has been observed in planar U-shaped plasmonic particles, like the well-known split-ring resonator geometry.[78] Furthermore, the absorbance peaks in the wavelength range of 500–600 nm in Fig. 5(a) and (b) are associated with the electric-quadrupolar resonance formed by the out-of-phase vertical charge separation along the sidewalls of the Au-HNP (left inset in Fig. 5(a) and (b)).

Next, a two-dimensional square array of Au-HNPs with a 250 nm pitch was investigated. The absorptance spectra of the periodic samples with and without BARC are depicted in Fig. 5(c) and (d), for Ti layer thicknesses of 13, 20, and 40 nm. The two peaks in the absorptance spectra coincide with the assigned dipolar and quadrupolar resonances of a single Au-HNP. It is worth noting that the peak absorptance increases

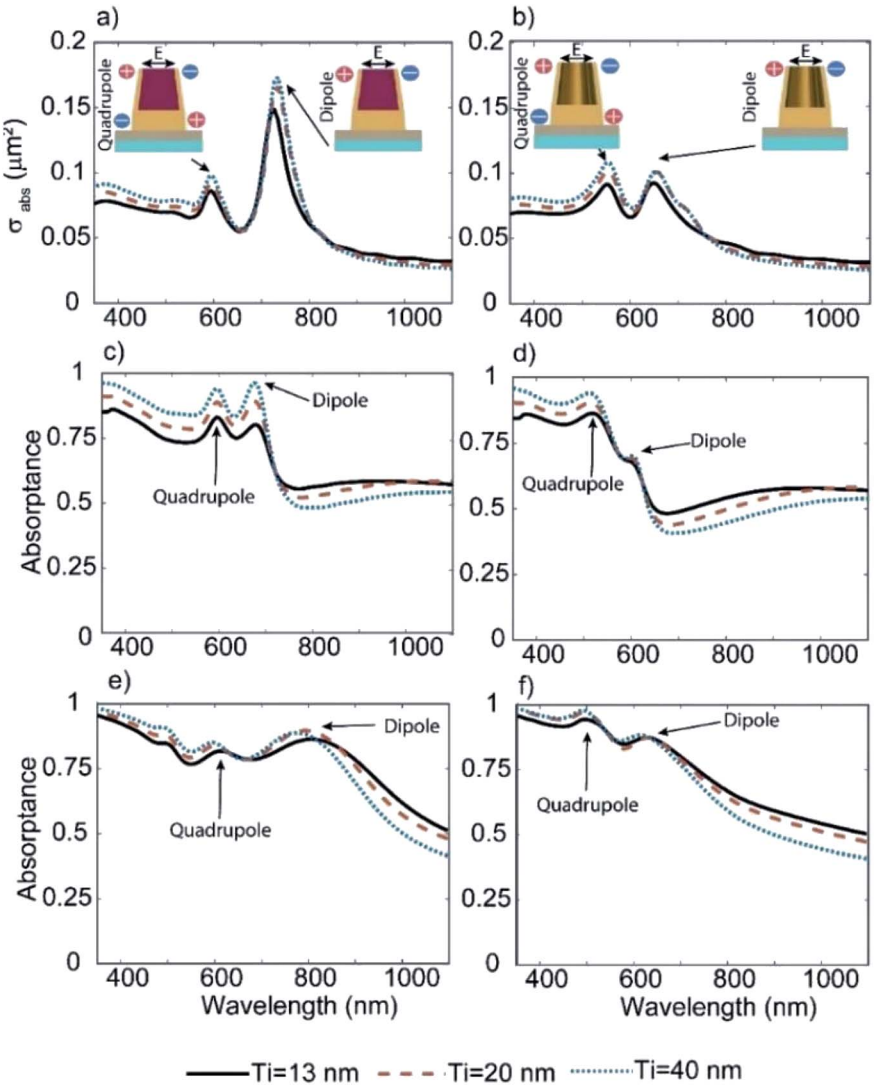

Fig. 5 Numerically calculated absorption cross-section for a single Au-HNP (a) with and (b) without BARC for Ti thicknesses of 13, 20, and 40 nm. The insets illustrate a schematic representation of the charge distribution of the supported modes. Numerically calculated absorption spectra of arrayed Au-HNPs (c) with and (d) without BARC for Ti thicknesses of 13, 20, and 40 nm. Measured UV-VIS-NIR-absorptance spectra of arrayed Au-HNPs (e) with and (f) without BARC for Ti thicknesses of 13, 20, and 40 nm.

with an increasing Ti layer thickness, especially for Au-HNPs with BARC. This is attributed to the larger reflection from the substrate in the samples with thicker Ti layers, consequently coupling more power to the modes.[79]

The measured UV-VIS-NIR-absorptance spectra of Au-HNPs with and without BARC for the different Ti thicknesses are presented in Fig. 5(e) and (f). The results show that the peaks are broadened and redshifted by $\Delta\lambda \sim 90$ nm if the nano-rim is filled with BARC. The resonance broadening of the dipole peak is attributed to increased optical losses and resonance inhomogeneity, likely caused by surface roughness and small variations in shape and dimension among the structures. The influence of these imperfections is not included in the simulations. It is worth mentioning that for single-crystalline Au-HNPs, narrower absorptance peaks are expected.[80]

It is well known that the resonance wavelengths of plasmonic particles are strongly dependent on their geometrical parameters. Thus, the effect of variations in the structural dimensions on the absorptance spectra is studied by employing FDTD simulations and factorial design analysis to understand the peak redshift observed in Fig. 5(e) and (f). The details can be found in the ESI file, Section 2.† The results of this study revealed that the thickness of the Au sidewall/nano-rim plays the dominant role in the redshift of the dipolar peak in comparison to the effects of other geometrical parameters, as shown in Fig. S11 and S12.† This is attributed to the increased length-to-width ratio of the sidewalls, which is a parameter known to affect significantly the resonance conditions of plasmonic nanostructures.[81,82]

The absorptance spectra of an array of Au-HNPs without BARC are calculated for different sidewall thicknesses, while other parameters remained constant to gain further insights into the redshift found for the electric dipole peak. The results in Fig. 6(a) and (b) show the dipole peak redshift as the sidewall thickness reduces, indicating a nonlinear dependency between the two quantities. It is also worth noting that small variations of ± 3 nm in the wall thickness (*ca.* 14 nm) result in a considerably large redshift of $\Delta\lambda \sim 90$ nm. Therefore, the sidewall thickness variations are primarily responsible for the redshift of the dipole peak in the experimental results, as depicted in Fig. 5(e) and (f). In addition, this variation because of the sidewall thickness is much larger than that due to variations in the thickness of the titanium adhesion layer or other geometrical aspects, as discussed in the ESI file Section 2.† Note that sidewall thicknesses > 20 nm will show no significant dipole peak contributions because of the dampened plasmonic response. As shown in Fig. 6(b), the relative shift in resonance wavelength reduces with the increasing sidewall thickness. Therefore, a thicker sidewall is expected to give more uniformity in the optical response because of the lower sensitivity to the sidewall thickness variations. However, despite fabrication challenges, a thinner sidewall is more appealing because of the increased absorption peak and the possibility of the spectral tunning of the peaks. This underlines the need for a controlled sidewall deposition, as presented in this paper.

3.3 Field enhancement in the Au-HNP array

Since the numerical and experimental results show surface plasmon resonance peaks in the absorptance spectra, it is interesting to investigate the field enhancement effect over the Au-HNPs. The intensity enhancement is calculated by $(|E|/|E_0|)^2$, in which E is the spatially dependent electric field, and $|E_0|$ is the electric field amplitude of the input source. The intensity enhancement in periodic samples at their corresponding dipolar resonances at $\lambda = 600$ and 680 nm for the Au-HNPs with and without BARC is shown in Fig. 7. Here, a relatively large intensity enhancement at the rim of the Au-HNPs is found. Consequently, the EF, which is proportional to $(|E|/|E_0|)^4$, is also large in these samples. An EF as large as $\sim 2 \times 10^5$ at 680 nm is obtained for the sample with BARC and a Ti thickness of 40 nm. This is twice as large as that for samples with thinner Ti, for example, 13 nm thick. The EF for all samples without BARC is $\sim 4 \times 10^4$ at $\sim$600 nm, and it is not affected by the variation of the Ti layer thickness. For the excitation wavelength of 785 nm, which is the option of choice mainly when dealing with biological specimens, the intensity enhancement of the samples with and without BARC is shown in Fig. 8. Although the dipole absorption peaks are far from 785 nm, a comparatively large EF of the order of 10^4 is numerically achieved for all the samples. Higher EFs could be obtained for samples with engineered

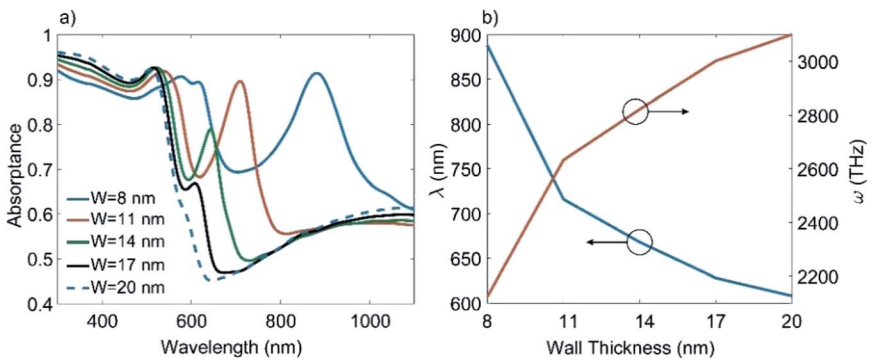

Fig. 6 (a) Absorptance spectra of an array of Au-HNPs without BARC for different sidewall thicknesses (W), while all other structural parameters are constant. (b) The dipole peak wavelength/frequency *versus* sidewall thickness.

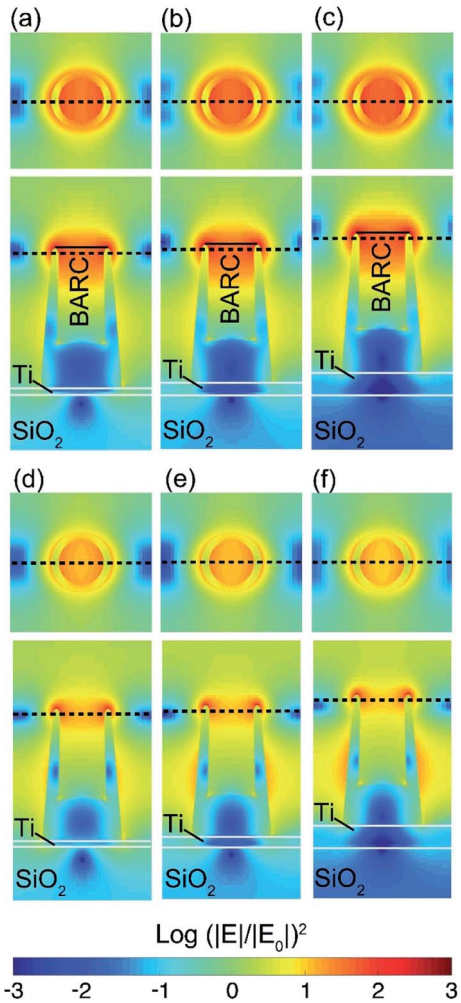

Fig. 7 Intensity enhancement $(|E|/|E_0|)^2$ for the samples with BARC and various Ti thicknesses of (a) 13, (b) 20, and (c) 40 nm at 680 nm. $(|E|/|E_0|)^2$ for the samples without BARC and various Ti thicknesses of (d). 13, (e) 20, and (f) 40 nm at 600 nm. The nanopillar size in the computational scheme is adopted from TEM images of real structures depicted in Fig. 4. A summary of the structural dimensions is shown in Fig. S7.†

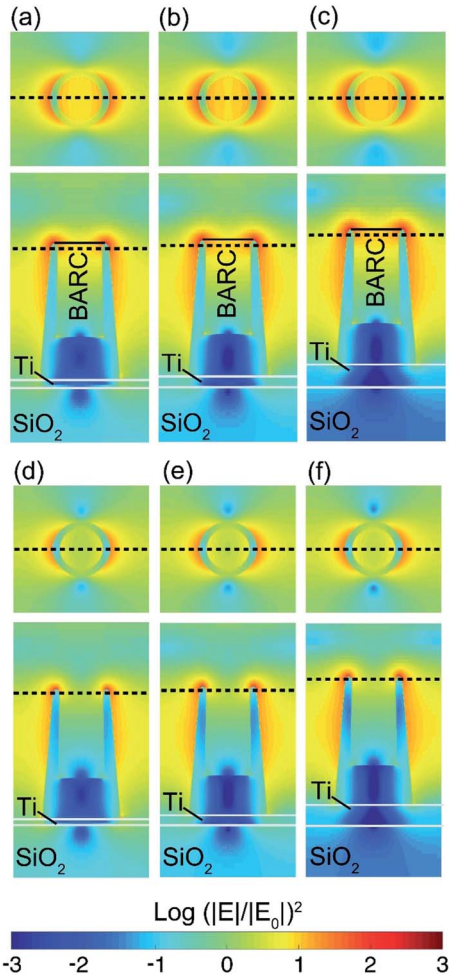

Fig. 8 Intensity enhancement $(|E|/|E_0|)^2$ for the samples with BARC and various Ti thicknesses of (a) 13, (b) 20, and (c) 40 nm at 785 nm. $(|E|/|E_0|)^2$ for the samples without BARC and various Ti thicknesses of (d). 13, (e) 20, and (f) 40 nm at 785 nm. The nanopillar size in the computational scheme is adopted from TEM images of real structures depicted in Fig. 4. A summary of the structural dimensions is shown in Fig. S7.†

geometries, *e.g.*, the addition of a silica shell[83] in which the dipole mode spectral region is shifted toward 785 nm.

3.3.1 Analytical enhancement factor using Raman spectroscopy of functionalized Au nanopillars. After exploring the optical response of the Au-HNP array using FDTD simulations, it is essential to compare the estimated EF values with the AEF. Confocal Raman spectroscopy experiments were conducted to compare the numerically predicted field enhancement with the AEF. AEF is a measure used in SERS but is now applied to compare our theoretical findings. For the estimation of AEF, methylene blue (MB) was used as the Raman reporter.[84–87] Raman spectra were recorded over Au-HNPs, and compared to an 80 nm flat sputtered Au layer functionalized with 1 mM of MB. For the AEF, measurements were conducted using a 10 μL droplet with a 1 mM aqueous solution MB deposited over the Au-HNPs. Raman spectra were recorded at the edge of the droplet.[62] It should be noted that 1 mM concentration is meant for AEF estimation and does not correlate with the Au-HNP detection limit. Information about the Au-HNP limit of detection for MB can be found in Fig. S13 and S14.† The minimum MB detectable concentration after functionalization was measured to be 100 nM. Furthermore, detection at laser powers as low as 5 μW was possible for Au-HNPs functionalized with 1 mM MB. This translates to an irradiance of 2.2 kW cm^{-2} in the case of 0.5 mW power and 22 W cm^{-2} in the case of 5 μW power which was calculated by considering the FWHM of the laser spot.

Fig. 9 shows the results for the conducted experiments using λ_{ex} of 633 and 785 nm. Peak assignment for MB is defined in Tables S3 and S4† for both λ_{ex}'s, and for the following MB Raman bands: 445, 1395, and 1618 cm^{-1} for $\lambda = 633$ nm, and 438, 1386, and 1629 cm^{-1} for $\lambda = 785$ nm. The Raman bands around 438 and 445 cm^{-1} are assigned to C–N–C skeletal deformation.[86,88] The bands at 1386 and 1395 cm^{-1} are

attributed to C–H in-plane ring deformation, and the bands at 1618 and 1629 cm^{-1} are designated to C–C ring stretching. The spectra collected on the bulk methylene blue powder, as presented in Table S3,† show none of the peak-splitting (doublets) and have much fewer peaks than the spectra recorded over the Au-HNP substrate, as presented in Fig. 9. For the AEF calculations, it is assumed to yield acceptable AEF values if solely the peaks measured on the bulk powder were compared to those also measured on the Au-HNPs. Considering peaks not present in the bulk powder but present over the Au-HNP would lead to spuriously large AEF. The steps taken to derive the AEF values are described in Section 2.6. It should be noted that for Au-HNPs not functionalized with MB, no Raman signal is observed. Furthermore, no Raman signal is found for bulk BARC and Au-HNPs with BARC and absence of MB even when using the highest laser power of 5 mW.

For the Raman bands in Table 1, an overall enhancement factor of $10^3 < AEF < 10^4$ is calculated in the case of the 633 nm excitation wavelength, which is slightly lower than predicted by the simulations. For the 13 nm substrate, the AEF is considered low, especially since the relative surface increase between the flat and structured unit cell is ~4.79, which means an increase in AEF compared to the flat surface may be entirely due to the increase in surface area. However, assuming at least a full monolayer coverage across the entire Au-HNP surface implies an averaged AEF acting on all molecules adhered to the surface.[89] Considering Fig. 7 and 8, it might well be that the SERS signal is generated only by MB molecules residing near the nano-rim, and the current calculation leads to an underestimation of the true enhancement factor. In the AEF calculations, the nano-rim area was ~1.2% of the total surface area.

Au-HNPs with 20 and 40 nm of Ti have increased performance in the case of λ_{ex} 633 nm. These substrates reveal an AEF larger than that which can be contributed to the Au-HNP relative surface area alone. The effect is attributed to the Ti layer thickness, which results in a more considerable reflection and a more efficient coupling to the plasmonic resonance of the Au-HNPs, enhancing SERS. Table 1 also contains the calculated values for AEF, $10^3 < AEF < 10^5$, in the 785 nm excitation wavelength. The calculated AEFs are larger for the 785 compared to the 633 nm excitation wavelength. Again, considering Fig. 7 and 8, the field intensity distribution yields a higher average value (*i.e.*, higher probed area) when evaluated along the sidewall edges for the wavelength of 785 nm. Such an effect can be responsible for the highest detected AEF using excitation at 785 nm.

Table 1 The Raman band, RB (cm^{-1}), and enhancement factors, AEF, for Au-HNPs (Ti = 13, 20, and 40 nm) and Au (flat) functionalized with 1 mM of MB at excitation λ = 633 nm and λ = 785 nm. All AEF values should be multiplied by 1000

Droplet	Ti = 13 nm		Ti = 20 nm		Ti = 40 nm		Au (flat)	
RB	RB	AEF	RB	AEF	RB	AEF	RB	AEF
λ = 633 nm								
445	440	0.5	446	3.1	447	5.2	447	0.2
1395	1387	1.0	1387	7.1	1390	9.9	1393	0.8
1623	1618	1.3	1618	8.6	1619	8.1	1618	0.3
λ = 785 nm								
438	444	10.8	440	48.4	438	22.4	438	1.1
1386	1390	2.5	1391	14.6	1390	4.4	1386	0.3
1629	1615	1.3	1609	36.7	1630	0.3	1630	0.2

Usually, the AEF calculation and reporting are done to compare the SERS properties of different SERS substrates. In that sense, the Au-HNP is best compared to other periodic Au arrays with MB functionalization. AEFs as high as 10^7 are found in the case of Au nanodisks functionalized with thiophenol.[90] Periodic Au nanogaps functionalized with benzenethiol lead to an AEF of 10^6.[91] In the case of functionalized nanoparticles and nanocuboids, a 10^5 AEF on rhodamine 6G with a 10^{-8} M detection limit has been found.[92] For nanocuboids, only the corners of the cuboid were considered for calculating the AEF. The AEF of 10^3 to 10^4 reported in this work is found by considering the whole area of the Au-HNPs. Chowdhury *et al.* stated a limit of detection of 10^{-10} M for MB functionalization with an AEF ~10^5. However, this system consists of Au nanoprisms immobilized on PS beads and is thus very different from the well-defined Au-HNP array.[93] If only the regions of high

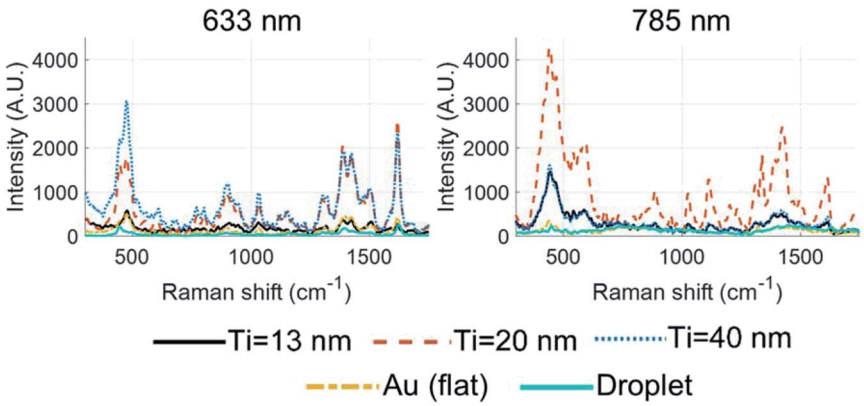

Fig. 9 Measured Raman spectra for Au-HNPs with various Ti thicknesses (13, 20, and 40 nm) and Au (flat). Raman spectrum for a deposited droplet of MB over Au-HNPs (Ti = 20 nm) is included. MB concentration utilized for these experiments is 1 mM.

electric field intensity were considered (the nano-rim of the Au-HNPs) the AEF in our work increases by a factor of 10^2. Finally, to the best of our knowledge, the results indicate that the Au-HNP substrates have SERS properties and perform similarly to other reported structures.[90–93]

Regarding the Au-HNP array, the measured AEF can be further increased by optimizing the structural dimensions or periodicity. The FDTD model can facilitate the rational design of Au-HNPs to improve SERS characteristics. For example, the sidewall thickness can be used to tune the absorptance peak location of the Au-HNP to the excitation wavelength which can be done by altering the exposure time during the sputter deposition and/or IBE redeposition. Furthermore, a combination of the shrinkage etching of BARC with sidewall redeposition can tune the diameter of the Au-HNPs. Moreover, a phase-shift mask with different periodicities or another lithographic technique like EBL can further tailor the spatial organization and periodicity of the Au-HNP array. In the future, we aim to fabricate Au-HNPs for both nanoplasmonic sensing and spectroscopy using the versatility offered by the pattern-ability of the hybrid lithography in combination with the sputter redeposition technique.

Conclusions

SHL was used to enhance and control the pattern-ability of a DTL-derived photoresist pattern. The combination of DTL/SHL with a sputter redeposition technique confines the periodic Au-HNPs, which are arranged in a square lattice with 250 nm pitch, to specific μm^2 to cm^2 sized areas over the wafer, paving the way for future complex device integration. The structures consisted of an 80 ± 2 nm thick solid base with a 170 ± 10 nm tall nano-rim structure on top. By performing sputter-redeposition at an oblique angle, control over the sidewall thickness was gained, and 14 ± 3 nm thick sidewalls were obtained. FDTD simulations demonstrate that the optical response in the visible and near-infrared spectrum was dominated by plasmonic resonances (quadrupole and dipole). We have combined a factorial design with FDTD simulations to underpin the redshift of the electric dipole peak. The results reveal that a ± 3 nm variation in the Au-HNP nano-rim thickness affects the surface plasmon resonance frequencies leading to a significant redshift up to $\sim$90 nm. This design aspect showed to be much more important than other aspects, such as the thickness of the Ti adhesion layer. These observations highlight the importance of control over the dimensions enabled by this fabrication method. Furthermore, we have demonstrated the potential of the fabricated Au-HNPs for SERS by employing MB as a probe analyte. We estimate the AEF to be *ca.* $10^3 < AEF < 10^4$ and *ca.* $10^3 < AEF < 10^5$ for λ_{ex} of 633 and 785 nm. The AEF can be further increased by optimizing the geometry of Au-HNPs for the best SERS response. The fact that the numerical and experimental results agree well discloses the FDTD simulation potential for optimization of the optical response. We expect that Au-HNPs will find application in the fields of nanoplasmonic sensing and spectroscopy.

Conflicts of interest

There are no conflicts of interest to declare.

Acknowledgements

The authors would like to thank Henk Van Wolferen, Mark Smithers, and Rico Keim for their assistance during specimen preparation and SEM, and TEM image collection. Prof. Monica Morales Masis and Dr Yuri Smirnov are acknowledged for laboratory access and help during UV-VIS-NIR-experiments. Dr Hai Le-The is acknowledged for fruitful discussions. D. J. and H. G. thank the Netherlands Center for Multiscale Catalytic Energy Conversion (MCEC), an NWO Gravitation program, funded by the Ministry of Education, Culture and Science of the government of the Netherlands. I. D. L. and Z. J. acknowledge the financial support from CONACyT Grant No. CN-17-109 and the Federico Baur Endowed Chair in Nanotechnology. Part of the research leading to the results in this contribution has received funding from the European Research Council (ERC) under the European Union's Horizon 2020 research and innovation program (Grant agreement No. 742004).

References

1 W. L. Barnes, A. Dereux and T. W. Ebbesen, *Nature*, 2003, **424**, 824–830.
2 C. Ciracì, R. T. Hill, J. J. Mock, Y. Urzhumov, A. I. Fernández-Domínguez, S. A. Maier, J. B. Pendry, A. Chilkoti and D. R. Smith, *Science*, 2012, **337**, 1072–1074.
3 C. D'Andrea, J. Bochterle, A. Toma, C. Huck, F. Neubrech, E. Messina, B. Fazio, O. M. Maragò, E. Di Fabrizio, M. Lamy De La Chapelle, P. G. Gucciardi and A. Pucci, *ACS Nano*, 2013, **7**, 3522–3531.
4 Z. Wang, B. Ai, Z. Zhou, Y. Guan, H. Möhwald and G. Zhang, *ACS Nano*, 2018, **12**, 10914–10923.
5 F. De Angelis, M. Malerba, M. Patrini, E. Miele, G. Das, A. Toma, R. P. Zaccaria and E. Di Fabrizio, *Nano Lett.*, 2013, **13**, 3553–3558.
6 R. Proietti Zaccaria, F. Bisio, G. Das, G. Maidecchi, M. Caminale, C. D. Vu, F. De Angelis, E. Di Fabrizio, A. Toma and M. Canepa, *ACS Appl. Mater. Interfaces*, 2016, **8**, 8024–8031.
7 F. Neubrech, D. Weber, J. Katzmann, C. Huck, A. Toma, E. Di Fabrizio, A. Pucci and T. Härtling, *ACS Nano*, 2012, **6**, 7326–7332.
8 J. A. Jackman, A. Rahim Ferhan and N. J. Cho, *Chem. Soc. Rev.*, 2017, **46**, 3615–3660.
9 J. Ma, X. Wang, J. Feng, C. Huang and Z. Fan, *Small*, 2021, **17**, 1–24.
10 F. A. A. Nugroho, I. Darmadi, L. Cusinato, A. Susarrey-Arce, H. Schreuders, L. J. Bannenberg, A. B. da Silva Fanta, S. Kadkhodazadeh, J. B. Wagner, T. J. Antosiewicz, A. Hellman, V. P. Zhdanov, B. Dam and C. Langhammer, *Nat. Mater.*, 2019, **18**, 489–495.
11 X. Wang, S.-C. Huang, S. Hu, S. Yan and B. Ren, *Nat. Rev. Phys.*, 2020, **2**, 253–271.

12 B. Yan, A. Thubagere, W. R. Premasiri, L. D. Ziegler, L. D. Negro and B. M. Reinhard, *ACS Nano*, 2009, **3**, 1190–1202.
13 A. Chauvin, M. Lafuente, J. Y. Mevellec, R. Mallada, B. Humbert, M. P. Pina, P. Y. Tessier and A. El Mel, *Nanoscale*, 2020, **12**, 12602–12612.
14 H. K. Lee, Y. H. Lee, C. S. L. Koh, G. C. Phan-Quang, X. Han, C. L. Lay, H. Y. F. Sim, Y. C. Kao, Q. An and X. Y. Ling, *Chem. Soc. Rev.*, 2019, **48**, 731–756.
15 H. Wei and H. Xu, *Nanoscale*, 2013, **5**, 10794–10805.
16 M. Lafuente, I. Pellejero, V. Sebastián, M. A. Urbiztondo, R. Mallada, M. P. Pina and J. Santamaría, *Sens. Actuators, B*, 2018, **267**, 457–466.
17 J. Henzie, S. C. Andrews, X. Y. Ling, Z. Li and P. Yang, *Proc. Natl. Acad. Sci. U. S. A.*, 2013, **110**, 6640–6645.
18 Y. Yang, Y. H. Lee, I. Y. Phang, R. Jiang, H. Y. F. Sim, J. Wang and X. Y. Ling, *Nano Lett.*, 2016, **16**, 3872–3878.
19 Y. H. Lee, W. Shi, H. K. Lee, R. Jiang, I. Y. Phang, Y. Cui, L. Isa, Y. Yang, J. Wang, S. Li and X. Y. Ling, *Nat. Commun.*, 2015, **6**, 1–7.
20 M. Lafuente, I. Pellejero, A. Clemente, M. A. Urbiztondo, R. Mallada, S. Reinoso, M. P. Pina and L. M. Gandía, *ACS Appl. Mater. Interfaces*, 2020, **12**, 36458–36467.
21 Q. Zhang, Y. H. Lee, I. Y. Phang, C. K. Lee and X. Y. Ling, *Small*, 2014, **10**, 2703–2711.
22 T. Udayabhaskararao, T. Altantzis, L. Houben, M. Coronado-Puchau, J. Langer, R. Popovitz-Biro, L. M. Liz-Marzán, L. Vukovic, P. Král, S. Bals and R. Klajn, *Science*, 2017, **358**, 514–518.
23 A. Shiohara, Y. Wang and L. M. Liz-Marzán, *J. Photochem. Photobiol., C*, 2014, **21**, 2–25.
24 M. Fan, G. F. S. Andrade and A. G. Brolo, *Anal. Chim. Acta*, 2011, **693**, 7–25.
25 D. E. Johnston, D. R. Strachan and A. T. C. Johnson, *Nano Lett.*, 2007, **7**, 2774–2777.
26 G. Yin, S. Bai, X. Tu, Z. Li, Y. Zhang, W. Wang, J. Lu and D. He, *Nanoscale Res. Lett.*, 2019, **14**, 168.
27 Q. Guo, M. Xu, Y. Yuan, R. Gu and J. Yao, *Langmuir*, 2016, **32**, 4530–4537.
28 S.-M. Yang, S. G. Jang, D.-G. Choi, S. Kim and H. K. Yu, *Small*, 2006, **2**, 458–475.
29 M. Cottat, N. Lidgi-Guigui, I. Tijunelyte, G. Barbillon, F. Hamouda, P. Gogol, A. Aassime, J. M. Lourtioz, B. Bartenlian and M. L. de la Chapelle, *Nanoscale Res. Lett.*, 2014, **9**, 1–6.
30 K. T. Arat, T. Klimpel, A. C. Zonnevylle, W. S. M. M. Ketelaars, C. Th. H. Heerkens and C. W. Hagen, *J. Vac. Sci. Technol., B: Nanotechnol. Microelectron.: Mater., Process., Meas., Phenom.*, 2019, **37**, 051603.
31 C. Mack, *Fundamental Principles of Optical Lithography*, The Science of Microfabrication, 2007.
32 Q. Zou, S. Mo, X. Pei, Y. Wang, T. Xue, M. Mayilamu and G. Qin, *AIP Adv.*, 2018, **8**, 085302.
33 N. Vogel, C. K. Weiss and K. Landfester, *Soft Matter*, 2012, **8**, 4044–4061.
34 P. A. Mosier-Boss, *Nanomaterials*, 2017, **7**, 1–31.
35 N. J. Greybush, I. Liberal, L. Malassis, J. M. Kikkawa, N. Engheta, C. B. Murray and C. R. Kagan, *ACS Nano*, 2017, **11**, 2917–2927.
36 W. J. Thrift, C. Q. Nguyen, M. Darvishzadeh-Varcheie, S. Zare, N. Sharac, R. N. Sanderson, T. J. Dupper, A. I. Hochbaum, F. Capolino, M. J. Abdolhosseini Qomi and R. Ragan, *ACS Nano*, 2017, **11**, 11317–11329.
37 S. Ni, M. J. K. Klein, N. D. Spencer and H. Wolf, *Langmuir*, 2014, **30**, 90–95.
38 J. F. Bryche, F. Hamouda, M. Besbes, P. Gogol, J. Moreau, M. Lamy de la Chapelle, M. Canva and B. Bartenlian, *Micro and Nano Engineering*, 2019, **2**, 122–130.
39 M. Nayfeh, in *Fundamentals and Applications of Nano Silicon in Plasmonics and Fullerines*, Elsevier, 2018, vol. 135, pp. 89–137.
40 Y. Chen, *Microelectron. Eng.*, 2015, **135**, 57–72.
41 J. S. Hwang and M. Yang, *Sensors*, 2018, **18**, 4076.
42 H. H. Solak, C. Dais and F. Clube, *Opt. Express*, 2011, **19**, 10686.
43 H. Le-The, E. Berenschot, R. M. Tiggelaar, N. R. Tas, A. van den Berg and J. C. T. Eijkel, *Adv. Mater. Technol.*, 2016, **2**, 1600238.
44 P. Chausse, E. le Boulbar, P.-M. Coulon and P. A. Shields, *Opt. Express*, 2019, **27**, 32037.
45 P. M. Coulon, B. Damilano, B. Alloing, P. Chausse, S. Walde, J. Enslin, R. Armstrong, S. Vézian, S. Hagedorn, T. Wernicke, J. Massies, J. Zúñiga-Pérez, M. Weyers, M. Kneissl and P. A. Shields, *Microsyst. Nanoeng.*, 2019, **5**, 52.
46 A. Susarrey-Arce, K. M. Czajkowski, I. Darmadi, S. Nilsson, I. Tanyeli, S. Alekseeva, T. J. Antosiewicz and C. Langhammer, *Nanoscale*, 2019, **11**, 21207–21217.
47 B. Gerislioglu, L. Dong, A. Ahmadivand, H. Hu, P. Nordlander and N. J. Halas, *Nano Lett.*, 2020, **20**, 2087–2093.
48 Z. Zhang, T. Deckert-Gaudig, P. Singh and V. Deckert, *Chem. Commun.*, 2015, **51**, 3069–3072.
49 L. V. Brown, H. Sobhani, J. B. Lassiter, P. Nordlander and N. J. Halas, in *ACS Nano*, American Chemical Society, 2010, vol. 4, pp. 819–832.
50 M. Dipalo, H. Amin, L. Lovato, F. Moia, V. Caprettini, G. C. Messina, F. Tantussi, L. Berdondini and F. De Angelis, *Nano Lett.*, 2017, **17**, 3932–3939.
51 L. P. Hackett, W. Li, A. Ameen, L. L. Goddard and G. L. Liu, *J. Phys. Chem. C*, 2018, **122**, 6255–6266.
52 J. A. Huang, V. Caprettini, Y. Zhao, G. Melle, N. MacCaferri, L. Deleye, X. Zambrana-Puyalto, M. Ardini, F. Tantussi, M. Dipalo and F. De Angelis, *Nano Lett.*, 2019, **19**, 722–731.
53 H. J. Jeon, H. W. Yoo, E. H. Lee, S. W. Jang, J. S. Kim, J. K. Choi and H. T. Jung, *Nanoscale*, 2013, **5**, 2358–2363.
54 B. X. E. Desbiolles, A. Bertsch and P. Renaud, *Microsyst. Nanoeng.*, 2019, **5**, 11.
55 W.-B. Jung, S. Jang, S.-Y. Cho, H.-J. Jeon and H.-T. Jung, *Adv. Mater.*, 2020, 1907101.
56 L. V. Jenni, L. Kumar and C. Hierold, *Microelectron. Eng.*, 2019, **209**, 10–15.
57 S. Steen, S. J. McNab, L. Sekaric, I. Babich, J. Patel, J. Bucchignano, M. Rooks, D. M. Fried, A. W. Topol,

J. R. Brancaccio, R. Yu, J. M. Hergenrother, J. P. Doyle, R. Nunes, R. G. Viswanathan, S. Purushothaman and M. B. Rothwell, *Microelectron. Eng.*, 2006, **83**, 754–761.
58 A. Star, T.-R. Han, V. Joshi, J.-C. P. Gabriel and G. Grüner, *Adv. Mater.*, 2004, **16**, 2049–2052.
59 A. F. Chrimes, K. Khoshmanesh, P. R. Stoddart, A. Mitchell and K. Kalantar-Zadeh, *Chem. Soc. Rev.*, 2013, **42**, 5880–5906.
60 M. R. Willner, K. S. McMillan, D. Graham, P. J. Vikesland and M. Zagnoni, *Anal. Chem.*, 2018, **90**, 12004–12010.
61 M. R. Bailey, A. M. Pentecost, A. Selimovic, R. S. Martin and Z. D. Schultz, *Anal. Chem.*, 2015, **87**, 4347–4355.
62 H. Le-The, J. J. A. Lozeman, M. Lafuente, P. Muñoz, J. G. Bomer, H. Duy-Tong, E. Berenschot, A. Van Den Berg, N. R. Tas, M. Odijk and J. C. T. Eijkel, *Nanoscale*, 2019, **11**, 12152–12160.
63 Q. Zhou and T. Kim, *Sens. Actuators, B*, 2016, **227**, 504–514.
64 H. J. Jeon, K. H. Kim, Y. K. Baek, D. W. Kim and H. T. Jung, *Nano Lett.*, 2010, **10**, 3604–3610.
65 P. H. C. Eilers, *Anal. Chem.*, 2003, **75**, 3631–3636.
66 T. O. Haver, *A Pragmatic Introduction to Signal Processing with Applications in Scientific Measurement*, CreateSpace Independent Publishing Platform, 3rd edn, 2017, pp. 1–121.
67 E. C. le Ru, E. Blackie, M. Meyer and P. G. Etchegoint, *J. Phys. Chem. C*, 2007, **111**, 13794–13803.
68 N. Narband, M. Uppal, C. W. Dunnill, G. Hyett, M. Wilson and I. P. Parkin, *Phys. Chem. Chem. Phys.*, 2009, **11**, 10513–10518.
69 P. T. Hang and G. W. Brindley, *Clays Clay Miner.*, 1970, **18**, 203–212.
70 Y. Song and L. Wang, *Microsc. Res. Tech.*, 2009, **72**, 79–84.
71 P. J. Westerik, W. J. C. Vijselaar, J. W. Berenschot, N. R. Tas, J. Huskens and J. G. E. Gardeniers, *J. Micromech. Microeng.*, 2018, **28**, 015008.
72 J. J. Cuomo, S. M. Rossnagel, H. R. Haufman and R. Komanduri, *Handbook of Ion Beam Processing Technology: Principles, Deposition, Film Modification, and Synthesis*, 1990, vol. 112.
73 H. Le-The, E. Berenschot, R. M. Tiggelaar, N. R. Tas, A. van den Berg and J. C. T. Eijkel, *Microsyst. Nanoeng.*, 2018, **4**, 1–10.
74 R. E. Lee, *J. Vac. Sci. Technol.*, 1979, **16**, 164–170.
75 L. Mehrvar, H. Hajihoseini, H. Mahmoodi, S. H. Tavassoli, M. Fathipour and S. M. Mohseni, *Nanotechnology*, 2017, **28**, 315301.
76 F. Frost, R. Fechner, B. Ziberi, D. Flamm and A. Schindler, *Thin Solid Films*, 2004, **459**, 100–105.
77 N. Toyoda, T. Hirota, I. Yamada, H. Yakushiji, T. Hinoue, T. Ono and H. Matsumoto, *IEEE Trans. Magn.*, 2010, **46**, 1599–1602.
78 I. de Leon, M. J. Horton, S. A. Schulz, J. Upham, P. Banzer and R. W. Boyd, *Sci. Rep.*, 2015, **5**, 1–9.
79 Y. Guo, S. Jiang, X. Chen, M. Mattei, J. A. Dieringer, J. P. Ciraldo and R. P. van Duyne, *J. Phys. Chem. C*, 2018, **122**, 14865–14871.
80 J. S. Huang, V. Callegari, P. Geisler, C. Brüning, J. Kern, J. C. Prangsma, X. Wu, T. Feichtner, J. Ziegler, P. Weinmann, M. Kamp, A. Forchel, P. Biagioni, U. Sennhauser and B. Hecht, *Nat. Commun.*, 2019, **1**, 150.
81 C. Rockstuhl, F. Lederer, C. Etrich, T. Zentgraf, J. Kuhl and H. Giessen, *Opt. Express*, 2006, **14**, 8827.
82 G. W. Bryant, F. J. García De Abajo and J. Aizpurua, *Nano Lett.*, 2008, **8**, 631–636.
83 A. Vanderkooy, Y. Chen, F. Gonzaga and M. A. Brook, *ACS Appl. Mater. Interfaces*, 2011, **3**, 3942–3947.
84 M. A. Bedics, H. Kearns, J. M. Cox, S. Mabbott, F. Ali, N. C. Shand, K. Faulds, J. B. Benedict, D. Graham and M. R. Detty, *Chem. Sci.*, 2015, **6**, 2302–2306.
85 S. Dutta Roy, M. Ghosh and J. Chowdhury, *J. Phys. Chem. C*, 2018, **122**, 10981–10991.
86 G. N. Xiao and S. Q. Man, *Chem. Phys. Lett.*, 2007, **447**, 305–309.
87 S. T. Sivapalan, B. M. Devetter, T. K. Yang, T. Van Dijk, M. V. Schulmerich, P. S. Carney, R. Bhargava and C. J. Murphy, *ACS Nano*, 2013, **7**, 2099–2105.
88 S. H. Seo, B. M. Kim, A. Joe, H. W. Han, X. Chen, Z. Cheng and E. S. Jang, *Biomaterials*, 2014, **35**, 3309–3318.
89 Y. Song and L. Wang, *Microsc. Res. Tech.*, 2009, **72**, 79–84.
90 J. F. Bryche, R. Gillibert, G. Barbillon, M. Sarkar, A. L. Coutrot, F. Hamouda, A. Aassime, J. Moreau, M. Lamy de la Chapelle, B. Bartenlian and M. Canva, *J. Mater. Sci.*, 2015, **50**, 6601–6607.
91 H. Le-The, J. J. A. Lozeman, M. Lafuente, P. Muñoz, J. G. Bomer, H. Duy-Tong, E. Berenschot, A. van den Berg, N. R. Tas, M. Odijk and J. C. T. Eijkel, *Nanoscale*, 2019, **11**, 12152–12160.
92 G. Das, M. Chirumamilla, A. Toma, A. Gopalakrishnan, R. P. Zaccaria, A. Alabastri, M. Leoncini and E. di Fabrizio, *Sci. Rep.*, 2013, **3**, 1–6.
93 E. Chowdhury, M. S. Rahaman, N. Sathitsuksanoh, C. A. Grapperhaus and M. G. O. Toole, *Nanotechnology*, 2021, **32**, 025506.